Contents lists available at **CEPM**

Computational Engineering and Physical Modeling

Journal homepage: www.jcepm.com

Investigation on the Seismic Performance of Joints with Different Shapes in Bridge Columns

Saleh Salehi Fereidouni[1*], Xiuli Du[2]

1. Ph.D. Student, Key Laboratory of Urban Security and Disaster Engineering of Ministry of Education, Beijing University of Technology, Beijing 100124, China
2. Professor, Key Laboratory of Urban Security and Disaster Engineering of Ministry of Education, Beijing University of Technology, Beijing 100124, China

Corresponding author: *salehsf86@yahoo.com*

https://doi.org/10.22115/CEPM.2022.321707.1197

ARTICLE INFO

Article history:
Received: 26 December 2021
Revised: 02 January 2022
Accepted: 04 January 2022

Keywords:
Seismic performance;
Joints;
V-shaped bridge columns;
Reinforced concrete.

ABSTRACT

This research is aimed to study the influence of multiform column angles on bridge columns and cap beam joints. Based on analytical results, changing angles from 0 to 10 didn't show considerable impact on displacement and acceleration of bridge models. Furthermore, The joints of cap beam didn't play a key role by different stress and strain. Beside this, vital assesses have seen around cap beam to column joints. The analytical data indicates that significant place is lower corner of joints through strengthening. It can guide to obviate reinforcing bars consumption at the cap beam or columns, which are using many materials and spending extra money. The software used in this study was Abacus. The model was a two column bridge bent that has one pedestal. The bridge was first designed in CSI Bridge software based on the AASHTO 2007 bylaw, then re-modeled in Abacus software, and finally the effect of 7 earthquake accelerograms in 3 modes of the pedestal angle in the cap-column beam node were analyzed.

How to cite this article: Salehi Fereidouni S, Du X. Investigation on the seismic performance of joints with different shapes in bridge columns. Comput Eng Phys Model 2022;5(1):01–18. https://doi.org/10.22115/cepm.2022.321707.1197

1. Introduction

In recent years, due to its architectural and aesthetic considerations, the utilization of bridges with V-shape pedestals has been increased [1–8]. Due to the difference in angles between the pedestals of the normal bridges and the bridges with V-shape pedestals, it is necessary to investigate the effect of variation of the angle between the pedestals of the normal bridges in compared to the bridges with V-shape pedestals [9]. Since the effect of this angle variation has been mainly investigated on the pedestals only, it is necessary to investigate this effect on the upper cap beam to address in future designs.

Also, recently, with the advancement of technology and consequently the advancement of the technology of construction of structural materials such as concrete, application of high performance concrete (HPC) has attracted the attention of many civil engineers [10–17]. For this reason, in this paper, high performance concrete was utilized in modeling materials.

Shahid et al. studied the application of pozzolanic materials in manufacture of high performance concrete in 2018. In their study, pozzolanic materials were used to improve the performance and compressive strength of the high performance concrete. They conducted research experimentally on different samples with varying percentages of different additives [18].

In 2017, Kannan et al. investigated the manufacture of HPC by ceramic scrap powder instead of pozzolans. They replaced 20-40% of the Portland cement with ceramic scrap powder in the test experimental samples [19].

In 2019, Yepes et al. studied the optimization of the use of HPC in the concrete pedestrian bridges. In their research, high performance concrete with different characteristic strengths was used and by calculating the final price for each specimen, 70 MPa strength concrete was identified as the most optimal HPC for bridge construction [20].

Jose Restrepo et al., in 2006 tested the seismic performance of a concrete bridge built from an HPC with 55 MPa strength in San-Francisco. They modeled a column of 35% of the factual sample in the laboratory and examined its seismic performance. Two types of bar were used in the specimens: the HPC and the ASTM A706 bar. They challenged the existing numerical and computational estimates to estimate the seismic performance of the use of HPC materials and showed that if the plastic joint length is not available, the actual structural performance estimates will be not possible in these columns after entering the plastic range [21].

The aim of this study is to investigate to the effect of column angle variation on cap-column beam joint nodes of the bridges with V-shape pedestals and reinforced concrete material using nonlinear finite element analysis by ABAQUS software.

2. Modeling

2.1. General specifications of models

The studied bridge is a concrete double-span bridge with continuous spans as well as has a pedestal consisting of two columns. Three specimens of this bridge were modeled, the difference being in the angles between the columns. The angle between the columns in these two models is

zero, 10 degrees. The bridge deck is 30 m long and the columns height is 9 m. The reason for choosing the angle from 0° to 10° was to choose an angle range for the pedestal in design that based on static linear analysis does not require the pedestal to be reinforced, so that the pedestal with the dimensions and the specified bar size could be used at both angles. As a result, the factor of dimension variation and steel consumption on the cap-beam would be eliminated. The concrete used is high performance concrete (HPC) with a compressive strength of 75 MPa. The concrete bridge was first modeled in CSI Bridge 2017 software and designed according to AASHTO 2007 bylaw and then modeled again in Abacus software. The basis of the analysis in Abacus software was seismic performance based on 7 selected accelerograms from the Berkeley University site. First, the gravity loads were applied to the bridge and general static analysis was performed in 1 sec. The selected accelerogram records were then scaled and combined according to the NEHRP guidelines and inserted into the structure. The analysis performed to apply the earthquake effect is the implicit dynamic analysis. The accelerogram was perpendicularly applied to the bridge deck. The deck-to-pedestal connection was modeled as a contact joint, non-slip as well as fully free connection, while two blocks were added to limit the displacement of the deck relative to the pedestal on the both sides of the cap-beam. As the effect of heat, expansion and shrinkage of concrete, as well as the effect of braking and dynamic movement of the cars loads were not considered, the deck to abutment connection was also considered as a pin.

The node examined in this structure was the pedestal and cap-beam connection node on the bridge pedestal. According to the software output results, in addition to examining the stress and strain results at the theoretical location of the node, the stress and strain results at the lower point of the node, the column and beam connection were also examined.

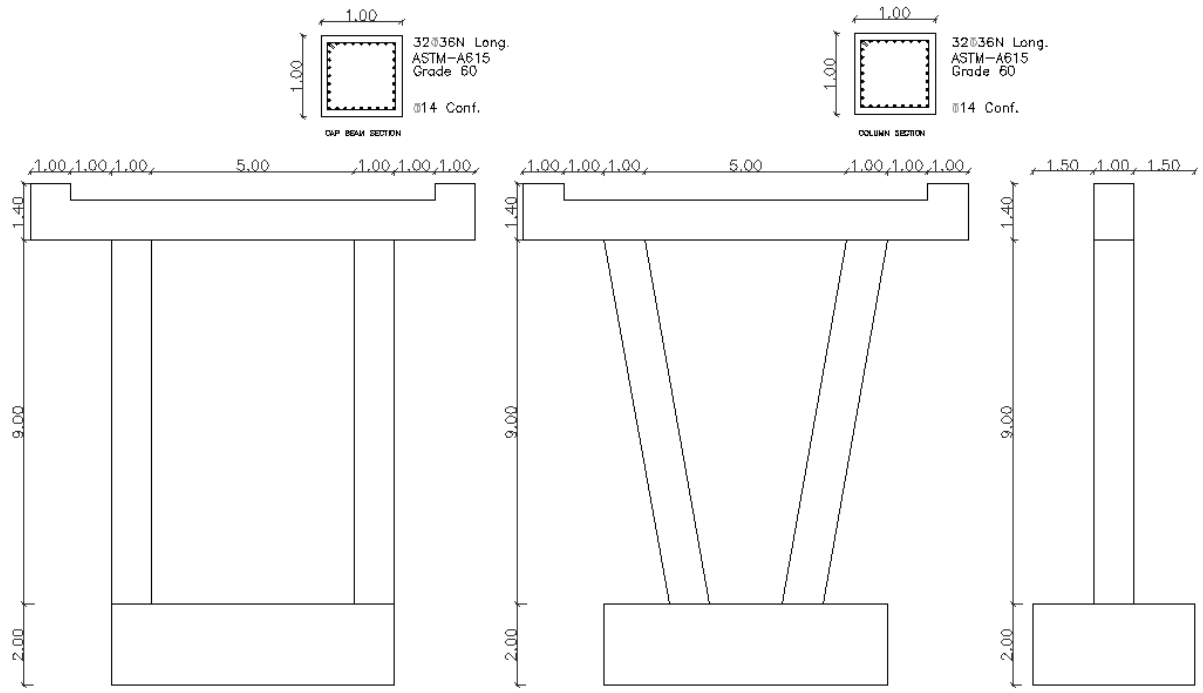

Fig. 1. The specifications of the models.

2.2. Materials specifications

Due to the sensitivity of the subject and the necessity to careful selection of materials as well as their accurate definition in the software, key and required parameters must be extracted and controlled. The concrete used in this research was the high performance concrete. The compressive strength of this concrete is 75 MPa. According to ACI 318-1999 regulations, the Young's modulus value is determined by the following equation:

$$\sqrt{f'_c}E = 4700 \tag{1}$$

The compressive strength of the standard cylinder sample is 75 MPa. Therefore, the Young's modulus would be 4.07 MPa.

It is very difficult to determine the concrete properties using only elastoplastic diagrams. One of the most important parameters required to precisely define concrete behavior is the concrete damaged plasticity (CDP) that could be obtained by loading and unloading on the cubic samples in the laboratory. Two damage mechanisms, including compressive and tensile damage, are determined according to Jason equations [22].

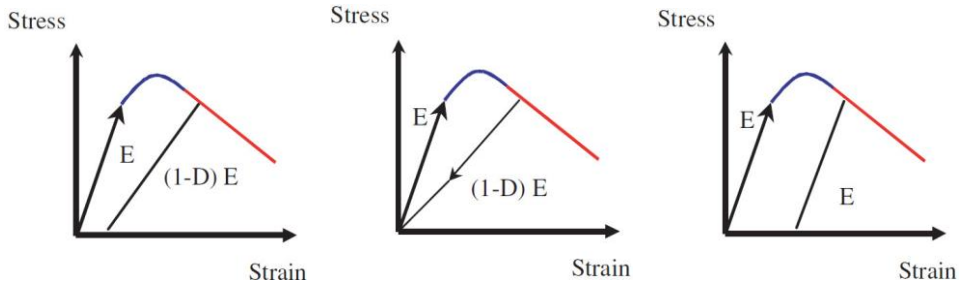

Fig. 2. Damage mechanisms of concrete [22].

As shown in Figure 2, the unloaded concrete sample is weakened and it could be said to have a low degree of hardness. The decrease in elastic hardness on the strain from the stress-strain diagram is characterized by two damage parameters, d_t and d_c. The indices t and c represent the tensile and compressive, respectively. These parameters are dependent on the plastic strain, temperature and environmental variables. The amount of damage varies from 0 to 1, which 0 indicate no damage and 1 indicate the complete damage. If E_0 is the non-reduced elastic hardness, then:

$$\sigma_t = (1 - d_t)E_0\left(\epsilon_t - \epsilon_t^{-pl}\right) \tag{2}$$

$$\sigma_c = (1 - d_c)E_0\left(\epsilon_c - \epsilon_c^{-pl}\right) \tag{3}$$

Accordingly, we could define the continuous effective stress for both tensile and compressive cases:

$$\bar{\sigma}_t = \frac{\sigma_t}{(1-d_t)} = E_0\left(\epsilon_t - \epsilon_t^{-pl}\right) \tag{4}$$

$$\bar{\sigma}_c = \frac{\sigma_c}{(1-d_c)} = E_0\left(\epsilon_c - \epsilon_c^{-pl}\right) \tag{5}$$

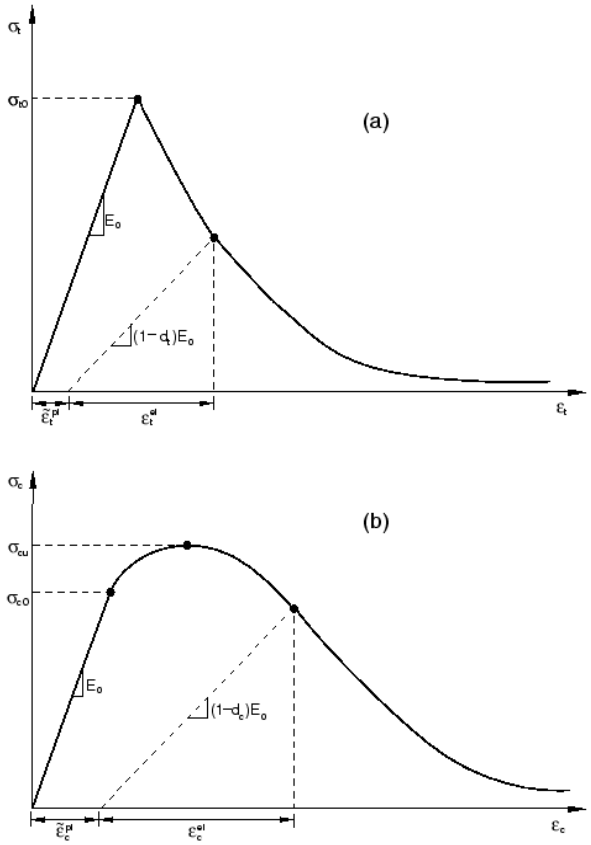

Fig. 3. Concrete response in uniaxial tensile (a) and (b) Compressive loading (ABAQUS software help).

Which this continuous effective stress indicates the surface yield (or failure).

The parameters defining the yield level include 4 different parameters in ABAQUS software. The Poisson's coefficient defines the volume change of concrete at stress values below the critical state which is defined using the following equation [23]:

$$v_c = 4.5 \times 10^{-7} w^{1.75} f_c^{0.5} \tag{6}$$

When the stress reaches a critical value, the concrete will increase in plastic volume [24]. This characteristic is defined by the angle of stretch. E is centrifugal which determines the asymmetry degree of the function (the potential current tends to the straight line while the centrifugal tends to zero). This value is 0.1 by default, indicating that the concrete has an almost constant stretch angle over a wide range of compressive stresses. σ_{b0}/σ_{c0} is the ratio of the biaxial yield stress to the uniaxial yield stress with a default value of 1.16 which is the recommended value of the software. K_c represents the constant ratio of secondary stress to the yield stress in half, which its default value is 0.667. The values of E, σ_{b0}/σ_{c0} and K_c should be determined by tri-axial test, but the purpose of this study is not to determine these three parameters. Also, as recommended by the software help, the default values in the modeling researches performed so far have been acceptable. Furthermore, according to Wittmann 1994 research, the viscose parameter value with the actual crack propagation mode in concrete is recommended to be 0.0001 and higher values are not recommended due to unrealistic crack propagation mode [25].

Table 1

Characteristics of the C75concrete used in this study.

f'	E	Poisson's ratio	Dilation Angle	Eccentricity	fb0/fc0	K	Viscosity Parameter	Peak Strain	Ultimate Strain	tensile strength	Critical Crack Opening
MPa	GPa	-	-	-	-	-	-	%	%	MPa	mm
75	40.6	0.2	30	0.1	1.16	0.667	0.0001	0.275	0.35	5.33	0.156

Table 2

Characteristics of the ASTM-A615 Grade 60 steel bar used in this study.

E GPa	Poisson's ratio	Fy MPa	Fu MPa	Max Elongation %
200	0.3	413	620	9

2.3. The forces applied on the models

First, the samples were modeled, analyzed, and designed in CSI Bridge 2017 software. The loads applied to models include dead loads of materials, traffic loads, and selective earthquake records. The criteria used in the design were in accordance with AASHTO 2007 bylaw, and the materials dead loads and the traffic loads were applied accordingly. At the same time, the status of the columns was controlled using accelerograms and FEMA P695 regulations. The design of the models, especially the bridge pedestals were performed in such a way that there was no need to change the column or bar cross-section, while none of the columns exceeded from the functional stage of continuous use of I.O in accordance with FEMA regulations. This is also the reason for choosing the maximum 10° angle for the columns. Because, if the columns cross-sectional dimensions or bar dimensions will also be deferent, final comparisons between models will be difficult and precise judgment of the angle effect cannot be obtained.

The traffic loads according to the AASHTO 2007 bylaws include an HL-93 truck load and a linear moving load with 3 meters width and the deck length of 9.3 kN/m, which will be combined at the most critical conditions.

The accelerograms were also selected based on a range of popular and common records as well as a combination of far-field and near-field faults records. The graphs and pseudo-acceleration values were extracted in 4-second according to the NEHRP instruction. After the scaling, the pseudo-acceleration averages were extracted and used in CSI Bridge as well as ABAQUS software. This is due to dramatic reduction in analysis time in both of software, while, reduce the number of graphs and making it easier to discuss and conclude models.

Table 3

Specifications of the accelerograms.

No.	Event	RSN	Distance km	year	mag
1	San Fernando	70	22	1971	6.5
2	Friuli	124	102	1976	6.5
3	Loma Prieta	792	68	1989	7
4	Cape Mendocino	828	8.5	1992	7.2
5	Landers	855	1.1	1992	7.3
6	Kobe	1102	3.4	1995	6.9
7	Hector Mine	1786	76	1999	7.1

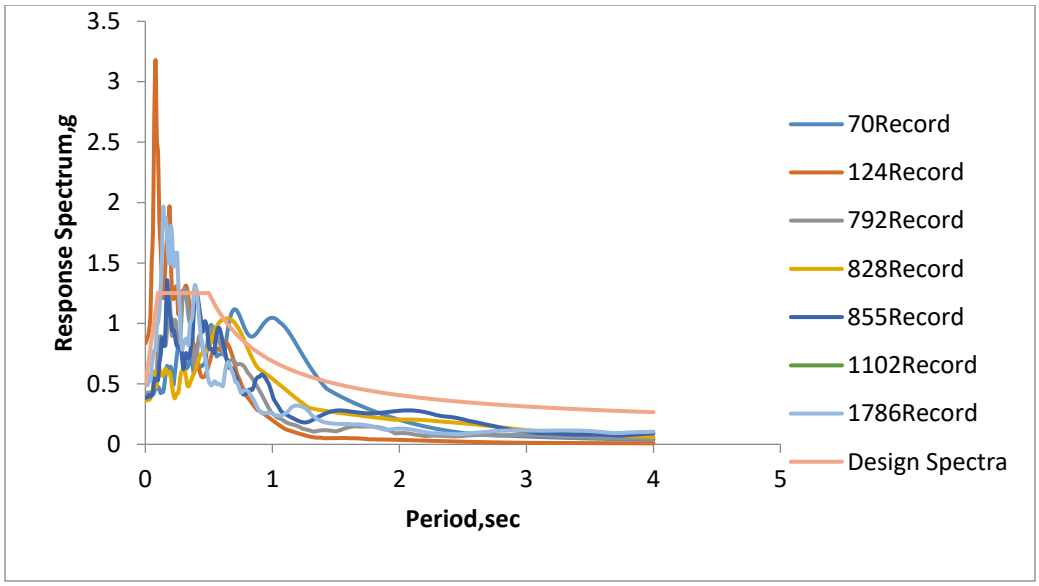

Fig. 4. Comparison of reflectance spectra of selected accelerograms.

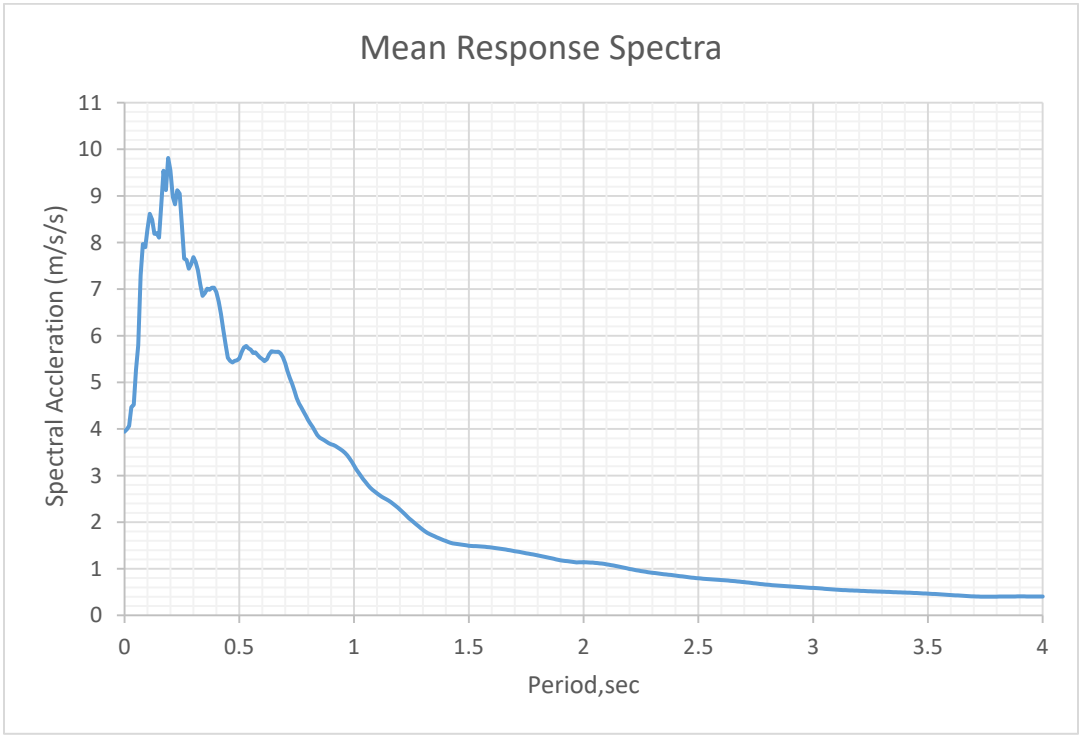

Fig. 5. Average response spectra of the selected and scaled accelerograms to gravity acceleration (9.81 m/s^2).

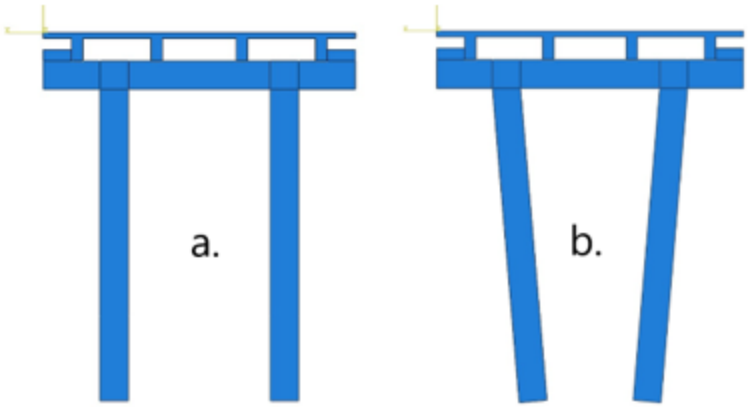

Fig. 6. The angle of columns (a) 0° and (b) 10°.

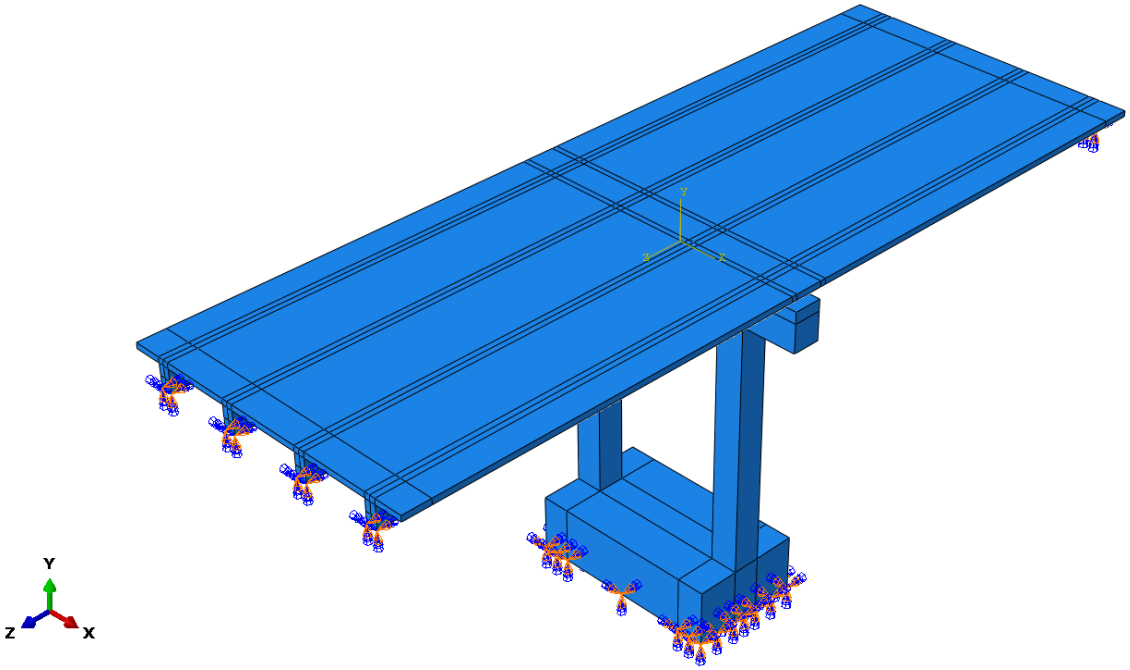

Fig. 7. 3D schematic of the 0° bridge (model 1).

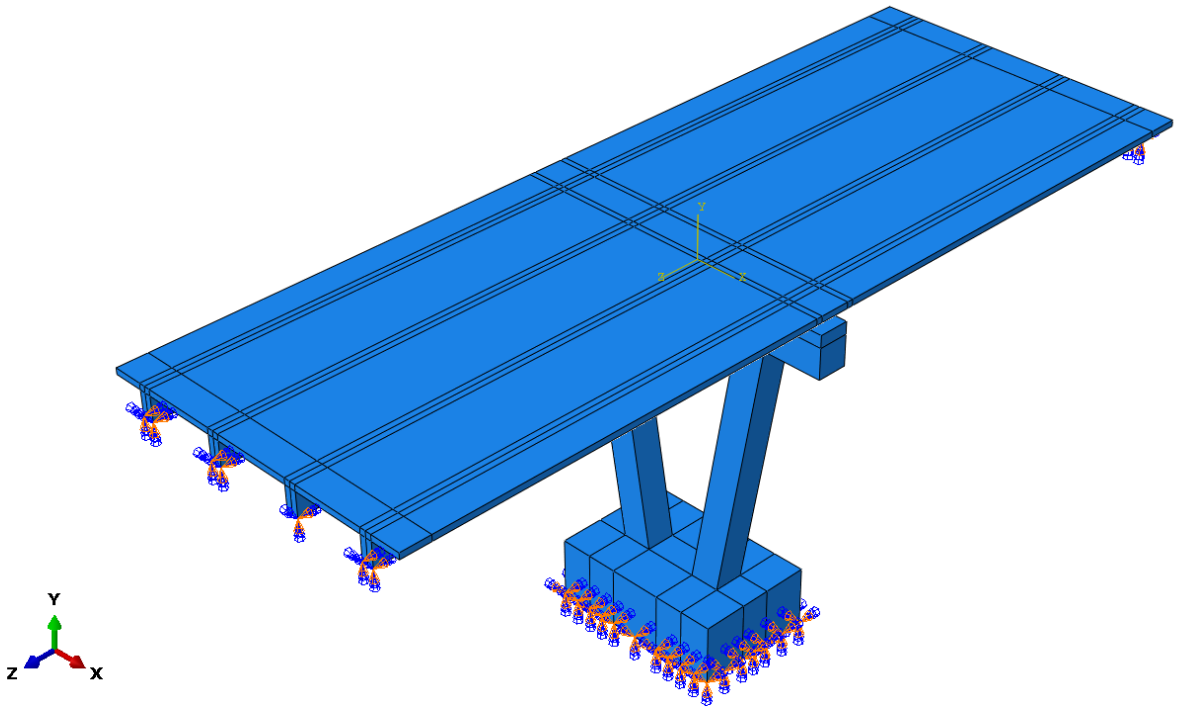

Fig. 8. 3D schematic of the 10° bridge (model 2).

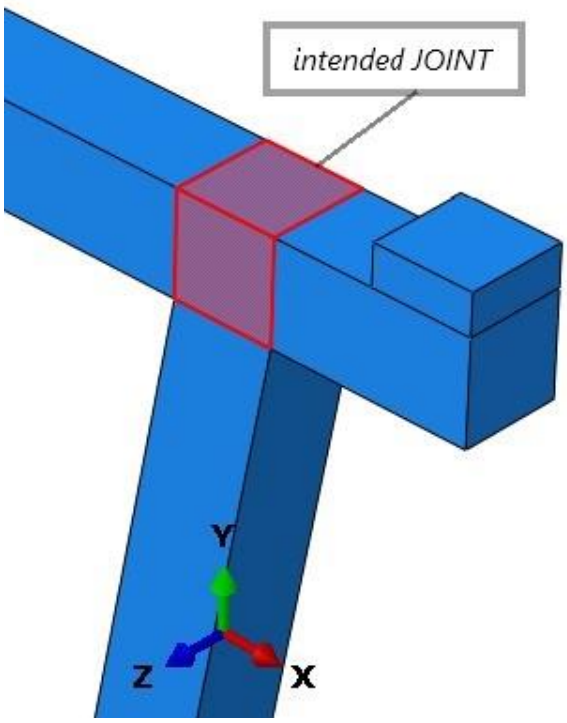

Fig. 9. The cap-beam and column joint in the pedestal.

The beam cap width and height was 1 m. Based on the analysis of two models with 2 column angles, the maximum displacement of the center of the deck mass was 19 cm in the first model and 24 cm in the second model.

3. Analysis

3.1. Linear analysis (reflectance spectrum with 0.5G scale)

As shown in Fig. 10, the stress-strain values in the bars around the cap beam-column joint node in Model 1 with a 0° column angle and model 2 with a 10° column angle were 18 MPa and 22 MPa, respectively. According to the values obtained by varying the angle from 0° to 10°, the maximum stress values increased by 18%.

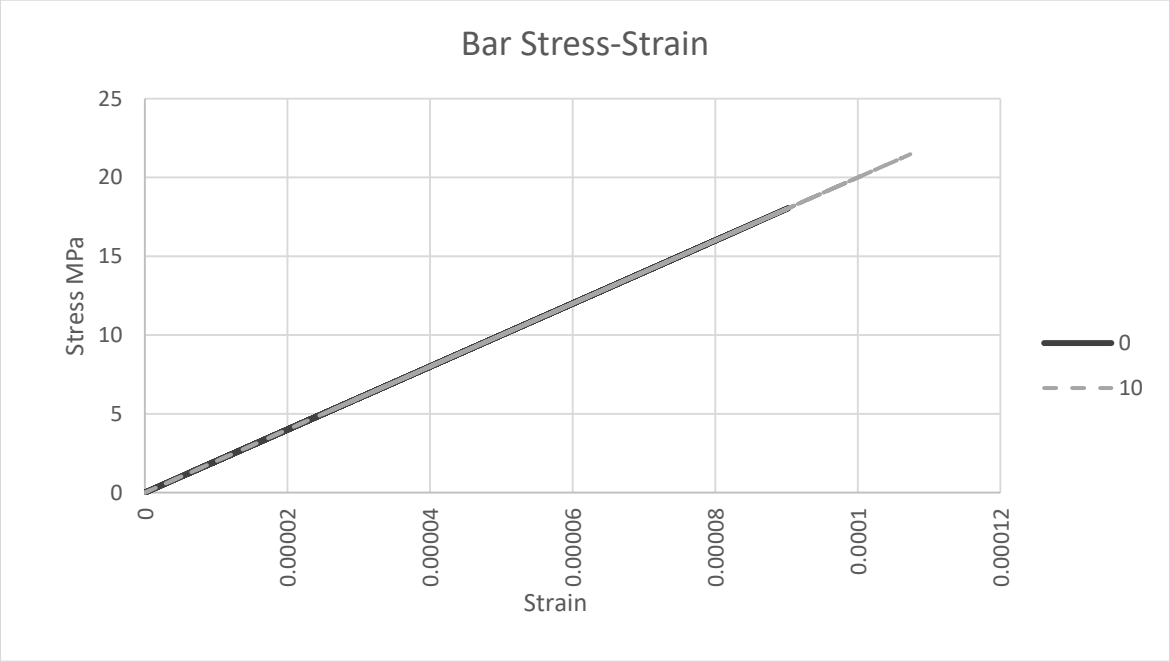

Fig. 10. Comparative stress-strain chart of the cap-beam bars (around the node).

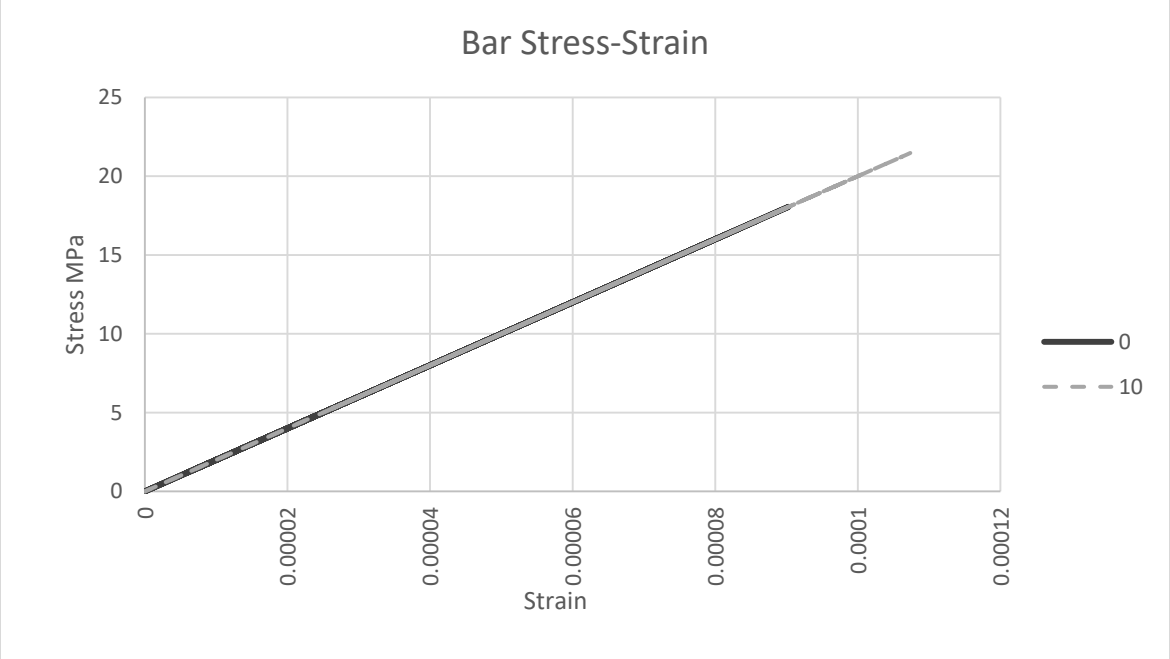

Fig. 11. Comparative stress-strain chart of the cap-beam concrete element (center the node).

As shown in Fig. 10, the comparative stress-strain diagram in the central point element of the joint node is affected by an earthquake measuring 0.5 g. According to this diagram, the elements in the joint node remain linear and the maximum stress in the first and second model is 21 MPa and 24 MPa, respectively. The column angle variation caused a 12% increase in the joint node stresses.

3.2. Nonlinear analysis (reflectance spectrum with g scale)

By applying the reflectance spectra at the g scale, both models have entered nonlinear ranges, causing more significant changes in the behavior of both models. First, we examine a number of parameters in the whole pedestal, and then we examine the main parameters such as stress and strain in the target node. By examining parameters such as the recovered strain energy and dissipated energy through the pedestal and then stress and strain values at the two ends of the columns, one can better judge the parametric variations in the cap beam-column joint node.

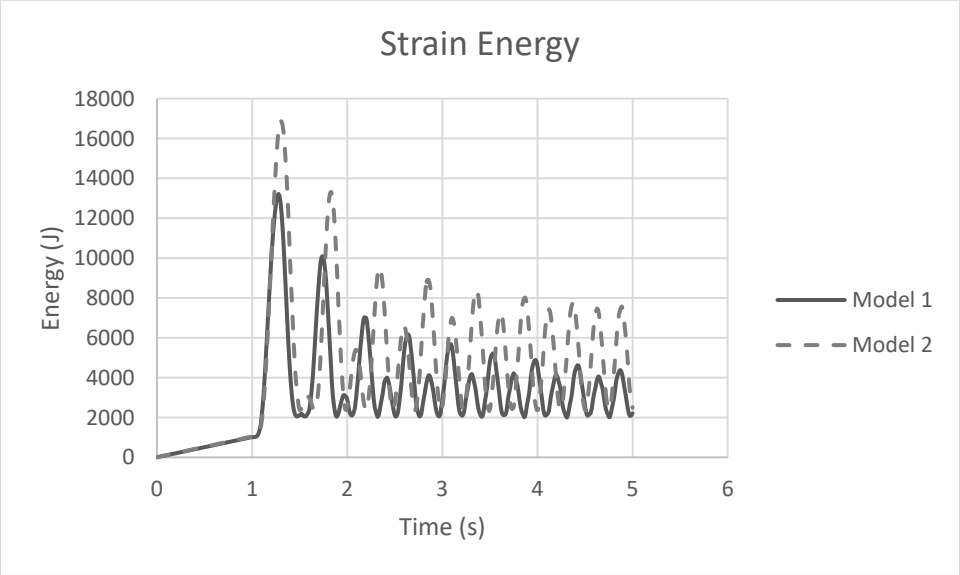

Fig. 12. The recoverable strain energy in the pedestal.

According to the Castigliano's first theorem, if the strain energy of the element is explained based on the external force, the element deformation will be along the applied force direction [26] which is defined by the following equation:

$$y = \frac{\partial U}{\partial P} \tag{7}$$

Which y is the deformation, U energy and P the external force applied to the element.

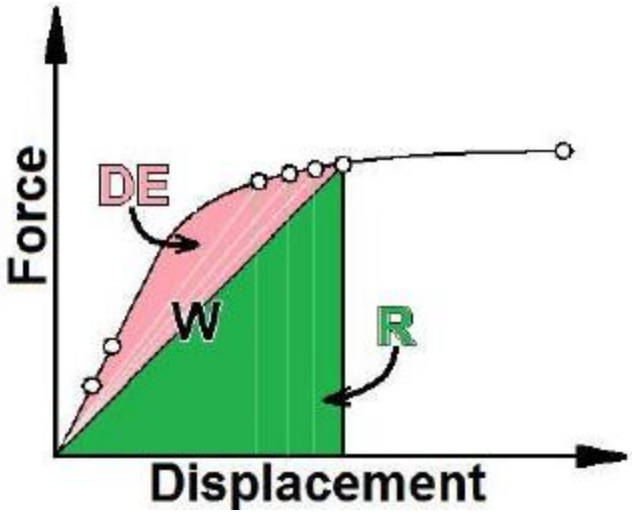

Fig. 13. The Force-Displacement diagram for the element.

According to this diagram, the R area represents the recoverable strain energy and the DE area represents the strain energy loss [27].

By definition, the strain energy means the energy that an element or a part absorbs as a result of deformation. As shown in Fig. 12, the recoverable strain energy in both models in the first second is approximately same under the influence of the gravity and traffic loads. With the onset of the earthquake load at the 1.23 second with an acceleration of 8.341 m/s2, the second model has begun to absorb more strain energy than the first model, reflecting more deformation in the second model elements. The maximum recoverable strain energy was 13216 joules in the first model and 16885 joules in the second model.

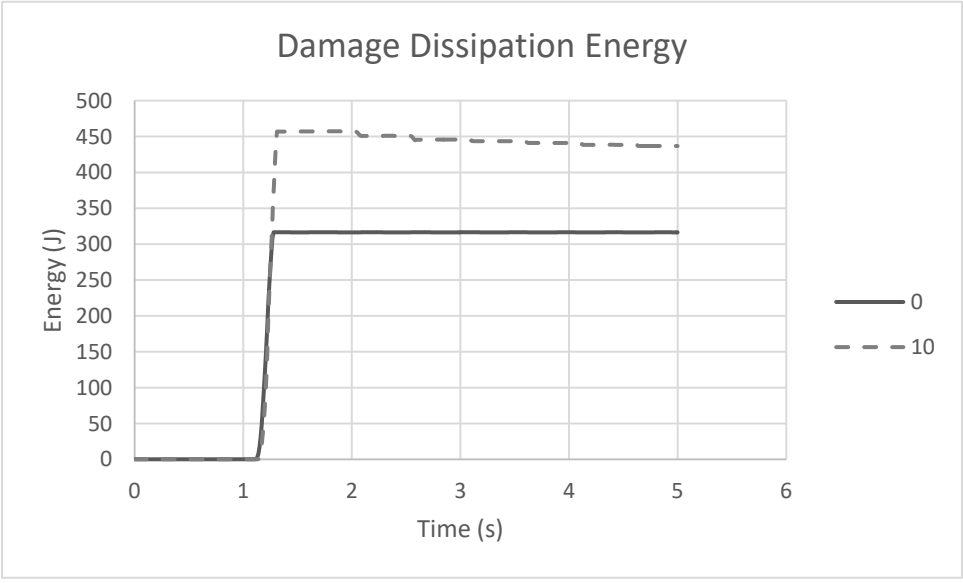

Fig. 14. Damage energy dissipation.

Figure 14 shows the dissipated energy arising from the elements damage. According to this diagram, the maximum energy dissipated due to damage is 318 joules in the first model and 457

joules in the second model. The dissipated energy due to damage and the recoverable strain energy indicate more damage of the second model in compared to the first one.

Another diagram to consider is the equivalent plastic strain curve. This graph is also called the von-Mises plastic strain chart. The stress-strain equation in the elastic domain is generally linear. After this range, the equation will be nonlinear. But it will not necessarily be inelastic. The plastic behavior occurs after the yield point stress in materials and is also referred as the non-recoverable stress or strain.

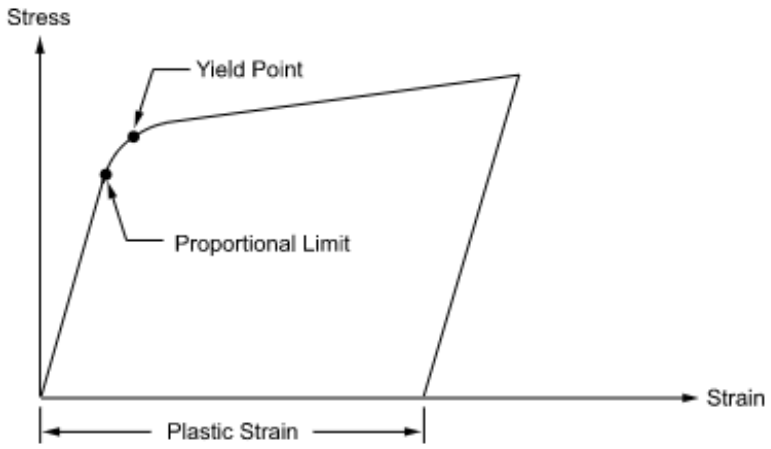

Fig. 15. Elasto-plastic (stress-strain) curve.

The Von-Mises (equivalent) stress is defined as a ratio of the three-axial (3D) stress in the element.

$$\sigma_e = \left[\frac{(\sigma_1-\sigma_1)^2+(\sigma_2-\sigma_3)+(\sigma_3-\sigma_1)^2}{2}\right]^{1/2} \tag{8}$$

The indexes represent three main directions of the element.

Equivalent (von Mises) strain is also defined according to a ratio of the tri-axial strain and effective Poisson coefficient:

$$\varepsilon_e = \frac{1}{1+v}\left(\frac{1}{2}[(\varepsilon_1-\varepsilon_1)^2+(\varepsilon_2-\varepsilon_3)+(\varepsilon_3-\varepsilon_1)^2]\right)^{\frac{1}{2}} \tag{9}$$

Which, the effective Poisson coefficient in the linear analysis is the Poisson coefficient at the reference temperature and it is 0.5 in the nonlinear analysis.

In both models, the equivalent plastic strain at the critical point of the cap beam-column joint node is represented in Figure 16.

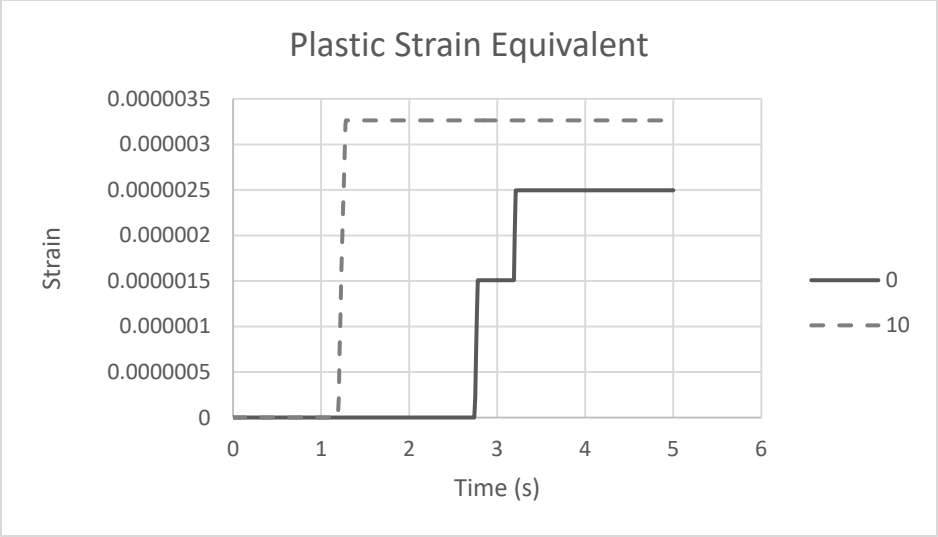

Fig. 16. The equivalent plastic strain at the joint node.

The mentioned point is located at the joint node and close to the beam-column joint plate. According to the above diagram, the equivalent plastic strain occurs at the second model joint node much prior to the first model and in the first and second model, it is $2.49E^{-6}$ and $3.26E^{-6}$, respectively.

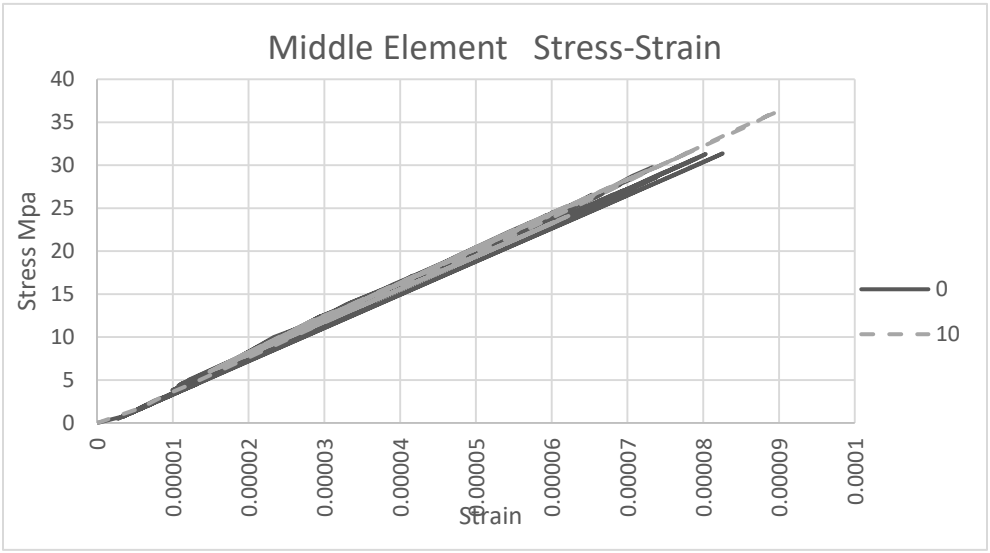

Fig. 17. The stress-strain curve in the joint node center.

In Figure 17, one could see the stress-strain relation at the joint node center. According to this curve, the behavior of both models is still linear. The maximum stress-strain values in the first and second models are 301 MPa, 8.22 E^{-5} and 36 MPa, 8.95 E-5, respectively.

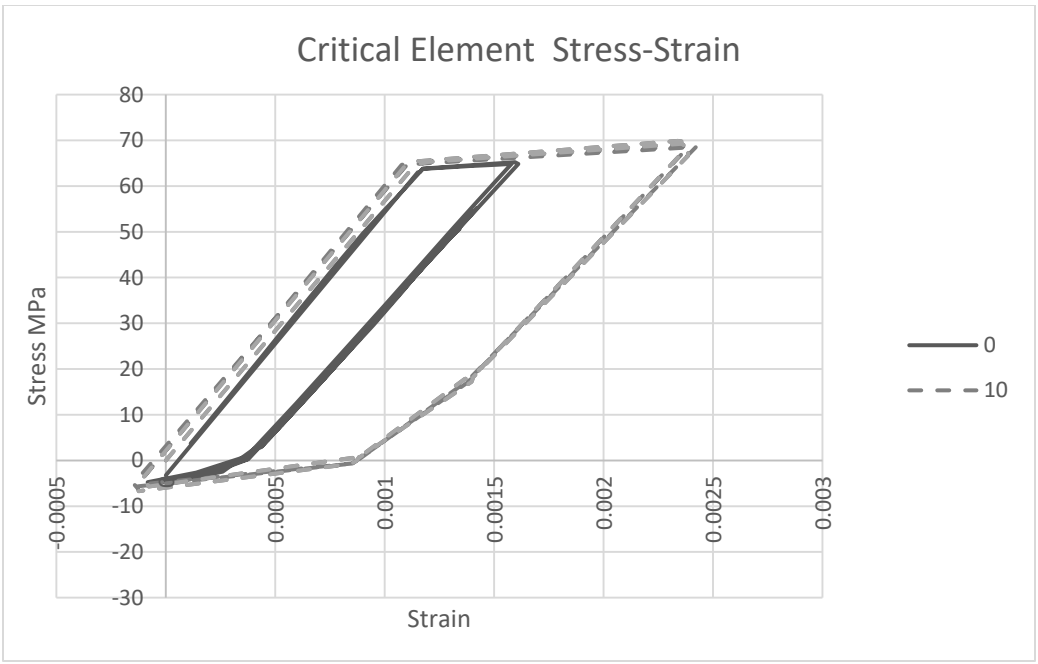

Fig. 18. The stress-strain curve at the critical point of the joint node.

Figure 18 shows the stress-strain curve at the critical point of the joint node (near the beam-column joint plate). According to this, the maximum compressive stress in the first and second models is 62 MPa and 70 MPa, respectively. The compressive stress variation in this element is 11%.

The maximum tensile stress in both models also is about 5.3 MPa as well as the damage percentage calculated by the software is zero.

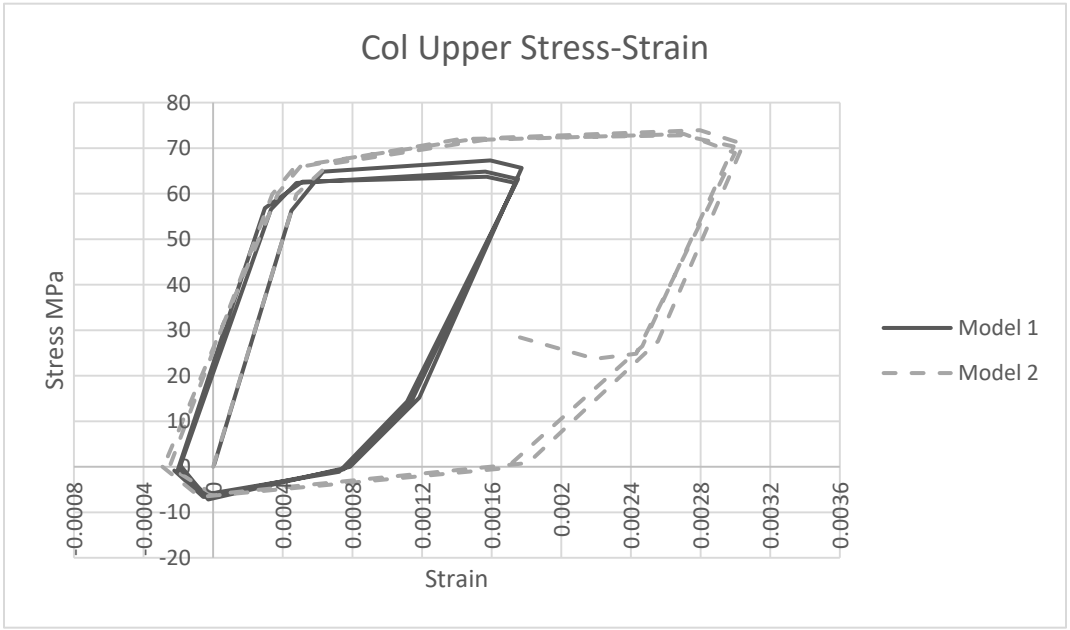

Fig. 19. The stress-strain curve of the upper critical element in the column (under the joint plate).

Fig. 19 shows the stress-strain curve of the upper critical element in the column. According to the curve in the first model, the maximum compressive and tensile stress is 67 MPa and 5.4 MPa, respectively. The element also enters the softening phase with 2% damage percentage. In addition, the maximum compressive and tensile stress in the second model is 74MPa and is 5.4 MPa with 10% damage percentage. The compressive stress variation in this element arising from the column angle change was only 9%.

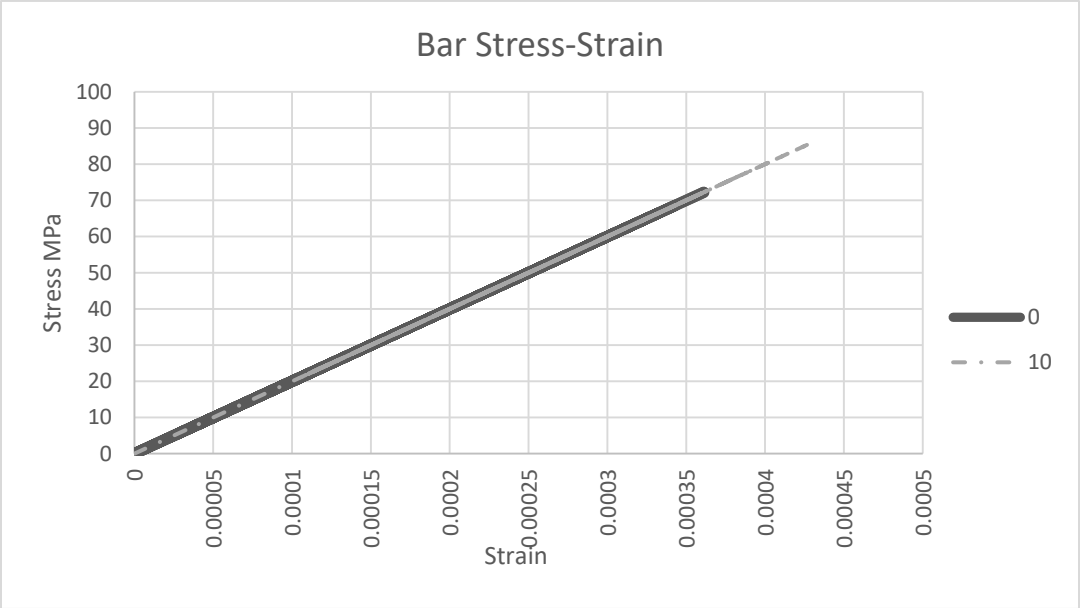

Fig. 20. The maximum stress-strain curve in the joint node bars.

As shown in Fig. 20, the bars located at the cap beam-column joint node remain in the linear range. The maximum stress in the first and second model bars is 73 MPa and 86 MPa, respectively. By variation of the column angle from 0° to 10°, the tension in the bars varied by only 15%.

4. Conclusion

Generally, the column angle variation at the bridge pedestal has a little effect on the theoretical center point of the beam-column joint node, while the external point on the cap beam-column joint plate is a critical point, which is the lower bound of the theoretical joint node. According to the results, when using the V-shape pedestal in bridges, the stresses and the concrete damage condition have to be controlled at the lower bound of the joint node. Especially in the commercial software used to design the bridge, the theoretical joint point is the criterion; which it could be designed to be applied to the maximum stress on the cap beam or column. In this case, with increasing the cap beam or column dimension, or increasing the amount of the rebar used in the structure, the design requirement is met. However, it is easier to prevent the increase in the volume of concrete and the amount of rebar used in the cap beam and column. One of these arrangements could be to add a concrete core to the beam-column joint plate (the upper column corner). In addition, the cross-sectional dimensions could be increased only in the

column head area, which increases the volume of concrete and rebar slightly in the structure and avoids additional costs.

References

[1] Phillippi DJ, Hegemier GA. Shear loading in two-column bridge bents. ACI Struct J 2014;111:1497.

[2] Lomiento G, Bonessio N, Benzoni G, Phillippi D, Hegemier GA. Capacity Assessment of V-Shaped RC Bridge Bents. J Bridg Eng 2014;19:266–80. https://doi.org/10.1061/(ASCE)BE.1943-5592.0000511.

[3] Black JS. Design and construction of small-scale bridge bents on drilled shaft foundations. MSE, Univ Texas Austin 2005.

[4] Xiang N, Alam MS. Displacement-based seismic design of bridge bents retrofitted with various bracing devices and their seismic fragility assessment under near-fault and far-field ground motions. Soil Dyn Earthq Eng 2019;119:75–90. https://doi.org/10.1016/j.soildyn.2018.12.023.

[5] Phillippi DJ, Hegemier GA. Simplified Two-Column Analytically-Based Fiber Model. ACI Struct J 2017;114:349.

[6] Franetović M, Mandić Ivanković A, Radić J. Seismic Assessment of existing bridges in Croatia. IABSE Symp. Rep., vol. 99, International Association for Bridge and Structural Engineering; 2013, p. 974–81.

[7] Xiao Y, Zhang Z, Hu J, Kunnath SK, Guo P. Seismic Behavior of CFT Column and Steel Pile Footings. J Bridg Eng 2011;16:575–86. https://doi.org/10.1061/(ASCE)BE.1943-5592.0000198.

[8] Li W, Huang C, Tang C. Negative Angle Vertical Rotating Construction Method of Reinforced Concrete Arch Bridge. Struct Eng Int 2017;27:558–62. https://doi.org/10.2749/222137917X14881937844847.

[9] Wang Y, Ibarra L, Pantelides C. Effect of incidence angle on the seismic performance of skewed bridges retrofitted with buckling-restrained braces. Eng Struct 2020;211:110411. https://doi.org/10.1016/j.engstruct.2020.110411.

[10] Yin W, Li X, Sun T, Wang J, Chen Y, Yan G. Experimental investigation on the mechanical and rheological properties of high-performance concrete (HPC) incorporating sinking bead. Constr Build Mater 2020;243:118293. https://doi.org/10.1016/j.conbuildmat.2020.118293.

[11] Akhnoukh AK. Accelerated bridge construction projects using high performance concrete. Case Stud Constr Mater 2020;12:e00313. https://doi.org/10.1016/j.cscm.2019.e00313.

[12] Sharma P. In-Situ Field Monitoring of a UHPC and HPC Bridge Superstructure under Diagnostic Load Testing Using Digital Image Correlation 2019.

[13] Darwin D, Khajehdehi R, Alhmood A, Feng M, Lafikes J, Ibrahim E, et al. Construction of crack-free bridge decks. University of Kansas Center for Research, Inc.; 2016.

[14] Van Dam T, Duffala N, Stempihar J. Phase I: Minimization of Cracking in New Concrete Bridge Decks. 2016.

[15] Alahmari TS, Kennedy CS, Cuaron AM, Weldon BD, Jáuregui D V. Field Testing of a Prestressed Concrete Bridge With High Performance and Locally Developed Ultra-High Performance Concrete Girders. Front Built Environ 2019;5. https://doi.org/10.3389/fbuil.2019.00114.

[16] Xia Y, Nassif H, Su D. Early-Age Cracking in High Performance Concrete Decks of a Curved Steel Girder Bridge. J Aerosp Eng 2017;30. https://doi.org/10.1061/(ASCE)AS.1943-5525.0000595.

[17] Reggia A, Sgobba S, Macobatti F, Zanotti C, Minelli F, Plizzari GA. Strengthening of a Bridge Pier with HPC: Modeling of Restrained Shrinkage Cracking. Key Eng Mater 2016;711:1027–34. https://doi.org/10.4028/www.scientific.net/KEM.711.1027.

[18] Irfan Ali Shahid Ali, SS. Mix-Design of high performance concrete (HPC) by using Pozzolanic material. NFC IEFR J Eng Sci Res Vol 6 2018.

[19] Kannan DM, Aboubakr SH, EL-Dieb AS, Reda Taha MM. High performance concrete incorporating ceramic waste powder as large partial replacement of Portland cement. Constr Build Mater 2017;144:35–41. https://doi.org/10.1016/j.conbuildmat.2017.03.115.

[20] Yepes V, Pérez-López E, García-Segura T, Alcalá J. Optimization of high-performance concrete post-tensioned box-girder pedestrian bridges. Int J Comput Methods Exp Meas 2019;7:118–29. https://doi.org/10.2495/CMEM-V7-N2-118-129.

[21] Restrepo JI, Seible F, Stephan B, Schoettler MJ. Seismic testing of bridge columns incorporating high-performance materials. ACI Struct J 2006;103:496.

[22] Jason L, Huerta A, Pijaudier-Cabot G, Ghavamian S. An elastic plastic damage formulation for concrete: Application to elementary tests and comparison with an isotropic damage model. Comput Methods Appl Mech Eng 2006;195:7077–92. https://doi.org/10.1016/j.cma.2005.04.017.

[23] Akçaoğlu T, Tokyay M, Çelik T. Effect of coarse aggregate size and matrix quality on ITZ and failure behavior of concrete under uniaxial compression. Cem Concr Compos 2004;26:633–8. https://doi.org/10.1016/S0958-9465(03)00092-1.

[24] Lee J, Fenves GL. A plastic-damage concrete model for earthquake analysis of dams. Earthq Eng Struct Dyn 1998;27:937–56. https://doi.org/10.1002/(SICI)1096-9845(199809)27:9<937::AID-EQE764>3.0.CO;2-5.

[25] Wittmann FH, Slowik V, Alvaredo AM. Probabilistic aspects of fracture energy of concrete. Mater Struct 1994;27:499–504. https://doi.org/10.1007/BF02473209.

[26] Srinivasa AR, Reddy JN. A model for a constrained, finitely deforming, elastic solid with rotation gradient dependent strain energy, and its specialization to von Kármán plates and beams. J Mech Phys Solids 2013;61:873–85. https://doi.org/10.1016/j.jmps.2012.10.008.

[27] Shyshko S, Mechtcherine V. Developing a Discrete Element Model for simulating fresh concrete: Experimental investigation and modelling of interactions between discrete aggregate particles with fine mortar between them. Constr Build Mater 2013;47:601–15. https://doi.org/10.1016/j.conbuildmat.2013.05.071.